Light Scattering and Wavefront Aberrations in In Vivo Imaging of the Rat Eye: A Comparison Study

Christian van Oterendorp,[1,2] *Luis Diaz-Santana,*[2,3,4] *Natalie Bull,*[4] *Julia Biermann,*[1] *Jens F. Jordan,*[1] *Wolf A. Lagrèze,*[1] *and Keith R. Martin*[4]

Purpose. In vivo imaging of the retina is becoming an increasingly important research method. General anesthesia rapidly compromises the corneal surface, which increases scattering. In addition, wavefront aberrations limit the maximum imaging resolution. Three common methods of stabilizing the air–cornea interface and reducing scattering are the use of a contact lens, a microscopy slide coverslip, or mineral oil. These methods have not yet been analyzed regarding their impact on scattering and wavefront aberrations.

Methods. Nineteen eyes of 19 rats were analyzed with a custom-made Hartmann-Shack (HS) wavefront sensor. The amount of scattering was determined by analysis of the HS spot width, and the wavefront was reconstructed for the naked eye and each scattering-reducing method. Their effect on optical quality was determined by calculating the modulation transfer function (MTF).

Results. The three methods applied significantly reduced scattering but were differentially effective, with the coverslip performing the best and the mineral oil the worst. The root mean square (RMS) of the wavefront aberration, as well as the intereye variability of the RMS, was significantly smaller with the contact lens than with the coverslip. The MTF was best for the contact lens and worst for the coverslip, which was also illustrated by image simulations.

Conclusions. The coverslip, contact lens, and mineral oil, when applied to the cornea, all reduced scattering. The best-performing method, the coverslip, increased wavefront aberrations. Overall, the contact lens had the best influence on image quality, and it appears to be the method of choice for high-resolution retinal imaging in rats. (*Invest Ophthalmol Vis Sci.* 2011;52:4551–4559) DOI:10.1167/iovs.10-6882

Recent years have seen a growing interest in in vivo imaging of rodent eyes to reveal microscopic retinal features in live animals under experimental conditions. Scanning laser ophthalmoscopes (SLOs),[1] confocal microscopes,[2] and fundus cameras[3] have been used for this purpose, mainly for fluorescence microscopy in live animals. Low-resolution images for cell counts can be acquired very quickly in awake animals.[4] Higher resolution imaging usually requires general anesthesia, which rapidly compromises the ocular surface tear film, thereby greatly increasing backward and, more important, forward scattering.[5,6] Satisfactory retinal image quality, regardless of the imaging technique, cannot be achieved without significantly reducing the scattering. Therefore, all publications on rodent in vivo imaging under anesthesia report some kind of air–cornea interface management. The most common approach is to use a microscopy slide coverslip placed on the cornea with a viscous watery interface for optical coupling.[1,2] Other studies have described the use of a contact lens, specifically designed to fit the rat corneal curvature, instead of a coverslip.[7,8] A different approach is to protect the cornea with mineral oil during image acquisition.[3] The effectiveness of these strategies has not been compared with regard to their ability to reduce scattering and their impact on optical aberrations.

Several psychophysical and optical methods have been developed to measure ocular forward light scatter.[9] They differ with regard to the scattering angle measured (small- versus large-angle scattering). Small-angle scattering affects the region of highest amplitude of the point-spread function (PSF; within 1° from the center), whereas large-angle scattering, also termed straylight, affects the region of low amplitude or periphery of the PSF (beyond 1° from the center).[10] The most widely used methods to quantify ocular small-angle scattering are either via a double-pass system[11,12] or by using images from a Hartmann-Shack wavefront sensor. The latter method, initially proposed by Applegate and Thibos,[13] has been validated and applied in several studies to quantify small-angle forward scattering: for example, cataract, keratoplasty, and increase in scattering with age[14–18] (Nam J, et al. *IOVS* 2010;51:ARVO E-Abstract 3947; Luque SO, et al. *IOVS* 2006;7:E-Abstract 1215).

Besides scattering, the presence of aberrations in the eye[7,5,19] is a major reason that conventional in vivo image resolution does not normally exceed the gross cellular level. Adaptive optics (AO) technology allows correction of aberrations[20] and has been successfully implemented in retinal imaging systems for humans and primates, providing unprecedented resolution and detail.[21–27] In rats, however, there is only one report on the use of an AO-SLO for retinal fluorescence imaging.[8] Alongside the technically demanding optical configuration of the rat eye (large numerical aperture and small entrance pupil), our knowledge about their optics, particularly wavefront aberrations, is much less comprehensive than our knowledge of humans and primates.[5,19] This lack of information makes it difficult to adequately use current AO technology to measure and correct wavefront aberrations.

In this report, we present data obtained from in vivo wavefront measurements of rat eyes. We compared the ability of the three common methods described above to reduce corneal

From the [1]University Eye Hospital Freiburg, Germany; the [3]Applied Vision Research Centre, City University London, United Kingdom; and the [4]Cambridge Centre for Brain Repair, University of Cambridge, United Kingdom.

[2]These authors contributed equally to the work presented here and should therefore be regarded as equivalent authors.

Supported by Imagine Eyes, which provided equipment and software loans.

Submitted for publication November 12, 2010; revised February 17 and March 27, 2011; accepted April 19, 2011.

Disclosure: **C. van Oterendorp**, Imagine Eyes, France (F); **L. Diaz-Santana**, Imagine Eyes, France (F); **N. Bull**, None; **J. Biermann**, None; **J.F. Jordan**, None; **W.A. Lagrèze**, None; **K.R. Martin**, None

Corresponding author: Christian van Oterendorp, University Eye Hospital Freiburg, Killianstrasse 5, 79106 Freiburg, Germany; christian.oterendorp@uniklinik-freiburg.de.

scattering and compared their impact on image formation and image quality, with emphasis on light-scattering and optical aberrations. With this work, we also wanted to supplement the current basic understanding of rat eye optics with quantitative data on light-scattering and wavefront aberrations, which is needed for the specific design of high-resolution imaging devices for these animals.

METHODS

Animal Handling

All animals used in this study were treated in accordance with the ARVO Statement for the Use of Animals in Ophthalmic and Vision Research. Nineteen male Sprague-Dawley rats between 13 and 21 weeks of age (mean, 17 ± 3 weeks; weight, 423.5 ± 14.2 g) were used. Measurements were taken only from the left eye.

All animals were anesthetized by isoflurane inhalation and kept warm by placement on a heating plate. Breathing and body temperature were constantly monitored. The right eye (not used for the experiment) was covered with lubricant eye gel (Corneregel Gel; Mann Pharma, Berlin, Germany). The left cornea was anesthetized with 1 drop of proxymetacaine 0.5% eye drops. Tropicamide 0.5% eye drops were subsequently used to dilate the pupil. To protect the cornea from dehydration, lubricant eye drops (Corneregel fluid; Mann Pharma, Berlin, Germany) were frequently instilled. Aberrations were measured as described below in the following sequence: naked eye (NK), coverslip (CS), contact lens (CL), naked eye (NK), and mineral oil (MO). The order of CS and CL was reversed in half of the animals, to avoid systematic errors, whereas the MO was always measured last, because remnants of the oil may have influenced the other measurements. The second measurement of the naked eye was intended as an internal control. All five measurements were collected during one experimental session.

The naked eye measurements (NK) were collected after instilling 0.9% sodium chloride in water solution drops to reduce scattering. Excessive liquid was carefully removed with a paper tissue. The CS was a standard microscopy slide cover (thickness, 0.130 mm; Glass BK7; VWR International, Lutterworth, UK), used only once for each eye and then discarded. It was carefully placed on top of the cornea, with carbomer eye gel (Corneregel gel; Mann Pharma) used for optical coupling. The cornea was not applanated. After the measurement, the CS was removed and discarded, the carbomer gel was washed out with 0.9% sodium chloride in water solution and lubricated with eye drops (Corneregel fluid; Mann Pharma), and excess liquid was removed.

The CL (Eyeart, Thessaloniki, Greece) was custom made (PMMA; front surface radius of curvature, $r = 3.253$ mm; back surface radius of curvature, $r = 3$ mm; apical distance = 0.34 mm). Carbomer eye gel was again used for optical coupling between the cornea and CL. After the wavefront measurements were collected, the eye was rinsed, and excessive water was carefully absorbed with a paper tissue placed in the conjunctival fornix without touching the cornea. Then, the second naked-eye measurement was performed. After data collection the CL was rinsed in distilled water and reused for all other eyes.

The MO used was baby oil (Johnson & Johnson, Langhorne, PA). Between one and three small drops were placed on the cornea, and care was taken to ensure an even distribution of the oil over the whole cornea. The aberrations were measured rapidly after instillation of the drops before breakup of the oil film became apparent. If needed, additional drops were applied.

Data Collection

A custom-made optical setup was built to measure scattering and wavefront aberrations. A Hartmann-Shack wavefront sensor (HASO; Imagine Eyes, Orsay, France) was coupled to the system and used to collect data.[28] The setup is shown in Figure 1. Lenses L1 and L2 formed

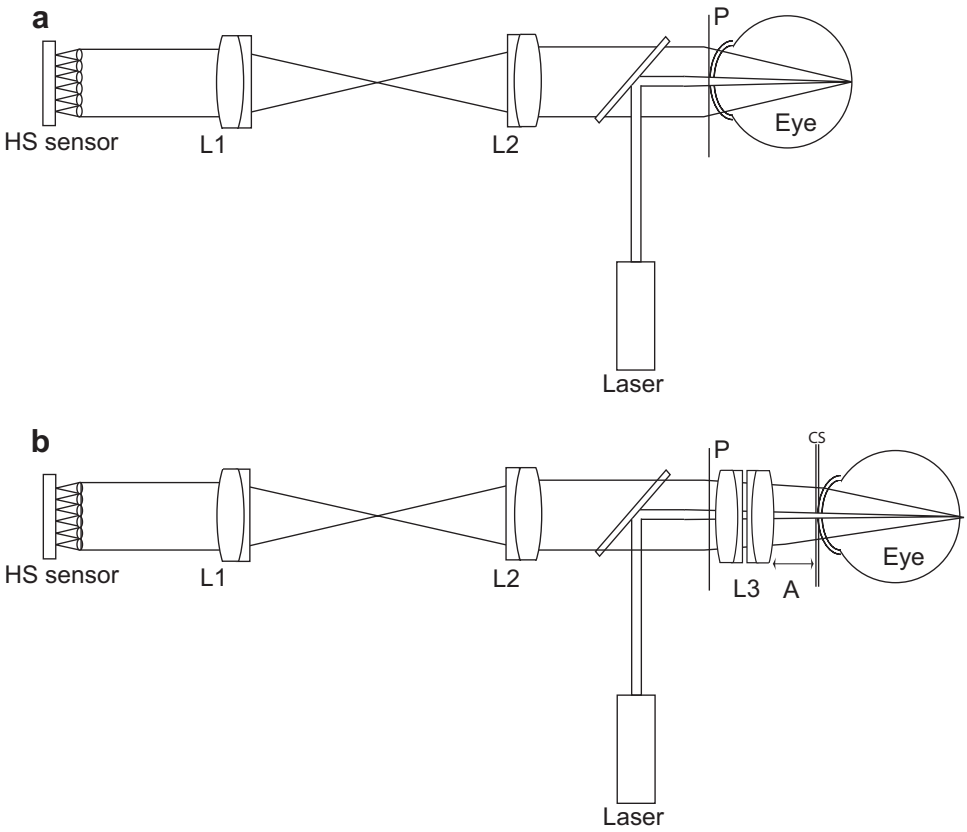

FIGURE 1. Measurement of wavefront aberrations. (**a**) Setup used for all measurements except the CS. (**b**) Setup used for the CS. L1, achromat f = 80 mm; L2, achromat f = 100 mm; L3, group of lenses formed by two achromats back to back 1 mm apart (the leftmost achromat in L3 f = 30 mm, rightmost achromat in L3, f = 40 mm). A, distance from rightmost surface in L3 to the CS. The incoming beam is collimated up to plane P. Diagram is not drawn to scale.

a 4-f telescope with magnification M = 0.8 conjugating plane P with the HASO sensor (HS). Lens (L3) in plane P was a removable group of lenses needed to correct for the loss in optical power induced by the use of a flat CS in front of the rat eye. For all other measurement conditions, L3 was removed, and the eye was moved forward to plane P (Fig. 1a). L3 consisted of two achromatic doublets with their flat surfaces facing each other, at a distance of approximately 1 mm (Fig. 1b). The achromat closest to the cornea had a 40-mm focal length, and the one farthest away, 30 mm. The CS lay on plane P1, at a distance *A* from the rightmost surface of L3. The distance *A* could be varied to ensure that the probing beam was best focused on the retina, thus minimizing defocus.

A collimated beam from a laser diode (LD), wavelength 650-nm diameter between 0.5 and 1.0 mm was injected into the system via a beamsplitter (BS). The beam was injected off center to avoid corneal reflections. The width of the injected beam was variable to control the intensity of the spots formed by the HS. The light reflected and backscattered from the retina traveled into the system and reached the HASO sensor on plane HS. The sensor was connected through an IEEE1394 interface to a computer (Intel MacBook; Apple, Cupertino, CA, running Windows XP-SP2; Microsoft, Redmond, WA). The system was calibrated without lens L3 and remained unchanged for all measurements. For data acquisition, the software provided by the HASO sensor permits a live visualization of the wavefront aberrations being measured. Using this feature, we moved the eye back and forth, varying the distance *A* until the defocus term was brought to a minimum. The axis of symmetry of the rat—defined by the line going from the snout to the tail—was placed at an angle of approximately 20° with the plane of the sensor's entrance pupil. By aligning that HS pattern with the center of the sensor, we ensured on-axis alignment with the system. Once the eye was in the correct plane and axis and the pattern of spots was centered on the HS detector, three individual Hartmann-Shack (HS) images were recorded for later analysis.

Data Analysis

Scattering Analysis. To measure the small-angle forward scatter we used the light spot images from the HS wavefront sensor, a method originally described by Applegate and Thibos.[13] In general, the shape of the PSF at small angles (<1° from center) is determined by higher order aberrations and scattering. Each spot in an HS sensor is a double-pass PSF, where the first-pass entrance pupil is defined by the injected beam (0.5 mm to 1 mm in our case) and the second-pass pupil by the aperture size of each lenslet in the HS (110 μm in our case).[29] In a well-designed HS sensor, both of these PSFs must be diffraction limited. Failure to fulfill these conditions renders the wavefront sensor data invalid for most applications.[20] As the second-pass aperture in our experiment was 5 to 10 times smaller than the first-pass one and the aberrations measured were relatively small, the shape of the HS spot was dominated by the PSF of the lenslet array and, excluding scattering, it should be invariant between measurements. Consequently, differences in the spot width are the result of differences in scattering, not in aberrations. The wider the HS spot the larger the amount of scattering present. Post hoc simulation with the data acquired from the 19 rat eyes ensured that within the conditions of our experiment, the influence on the HS spot width from the diameter of the laser beam or the defocus present was below the detection limit of our setup.

To quantify the HS spot width, the central 300 × 300 pixels of the HS images from each recorded image for each condition were selected. This square corresponds to ~88% of the 3.3-mm pupil area. In a region of 300 × 300 pixels, we typically found ~350 nontruncated HS spots.

The full width at half maximum (FWHM) has been used to quantify the HS spot width.[15] As the FWHM assumes a circular symmetry of the spots which, in our case, was not always true, we defined a metric analog to the FWHM and named it cross-sectional area at half maximum (CAHM). To illustrate the CAHM concept (Fig. 2), the spot intensity

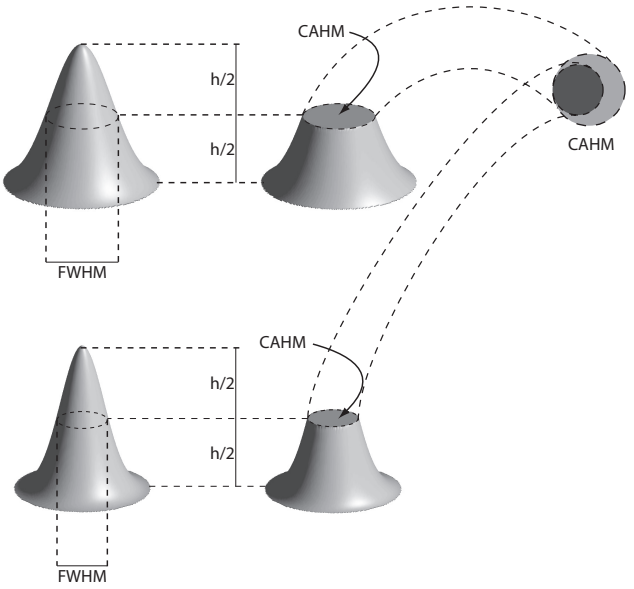

Figure 2. A representation of FWHM and CAHM in a high-scattering (*top*) and low-scattering (*bottom*) case.

distribution can be seen as a three-dimensional structure where the intensity defines its height (Fig. 2, far left). This structure is truncated at half its height, and the area at the section is the CAHM (Fig. 2, center). A narrow spot (less scattering) will have a smaller CAHM than a wider one (more scattering; Fig. 2 far right).

The CAHM was first calculated individually for each HS spot within the central 300 × 300 pixels of an HS image. The mean CAHM was then calculated. This process was repeated for each eye and experimental condition (6550 HS spots per experimental condition). The mean CAHM of all eyes in a single condition was then used as a measure for the scattering present in that condition (NK, CS, CL, or MO). The results for each experimental condition were compared by one-way ANOVA with post hoc Bonferroni correction for multiple comparison (95% CI).

The variability in the CAHM measurements was determined with a bootstrap algorithm. Hereby, the minimum–maximum difference was compared between the cases in 5000 paired bootstrap samples. The resulting *P* values were corrected for multiple comparison with a Bonferroni-Holm correction.

Wavefront Analysis. The image files recorded with the HASO sensor were extracted, and the wavefront slopes estimated from these images using an algorithm described by Talmi and Ribak.[30] From the wavefront slopes data, a modal reconstruction using a least-squares fit to the ANSI standard Zernike polynomial base (37 terms) was used.[28,31] All wavefronts were estimated over a 3.3-mm diameter circular pupil (~400 HS spots), as measured on plane P (Fig. 1). The wavefront root mean square error (or wavefront root mean square [RMS]) was calculated from the Zernike coefficients.[31] The estimated wavefront was reconstructed from the Zernike coefficients C_n, and the modulation transfer function (MTF) was calculated from the reconstructed wavefront.[32]

The individual Zernike polynomials and wavefront RMS were compared between the different experimental conditions (NK1, NK2 CL, CS, and MO). The comparison between individual Zernike polynomials was made with a one-way ANOVA with Bonferroni correction for multiple comparison, whereas the RMS, which does not follow a Gaussian distribution, was compared by using a Friedman test with the Dunn correction for multiple comparison. To test for statistically significant differences in the variability of the wavefront RMS, the same bootstrap algorithm as used in testing the variability in the CAHM was used.

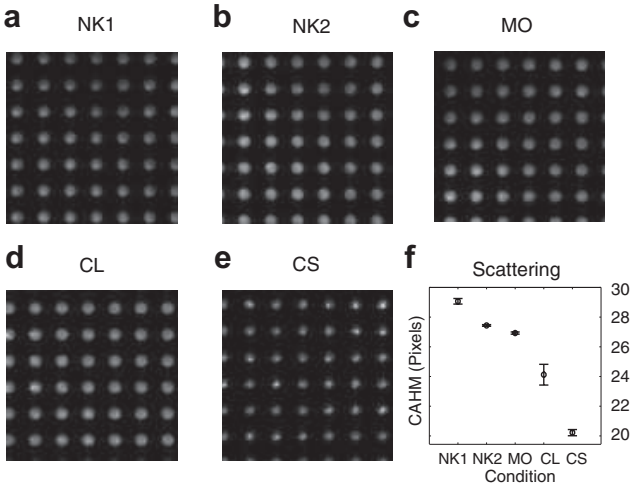

FIGURE 3. Scattering results. (**a–e**) Representative raw images of the HS spots showing differences in their width due to the scattering present. (**f**) Mean value of the CAHM for all different experimental conditions tested. Error bars, SEM, $n = 19$.

RESULTS

Scattering

Figures 3a–e show representative images of the HS spots in a small area close to the center of the pupil for each experimental condition. The HS spots obtained when using the CS appear to be the narrowest and best defined, whereas, for the other conditions, visual inspection alone did not show obvious differences.

Figure 3f shows the mean value of CAHM and its SEM for all experimental conditions. The highest amount of scattering was measured on the naked eye before all other measurements (NK1; 29.07 ± 0.188). Compared with this baseline (NK1), all conditions showed significantly less scattering. This included the second measurement of the naked eye (NK2) performed after the CL and CS measurement (27.44 ± 0.054; $P < 0.05$). Within the three air–cornea interface improvements, the CS (CS; 20.22 ± 0.21) performed clearly better than the CL (24.12 ± 0.697) and the MO (26.93 ± 0.074; $P < 0.0001$ for NK1 vs. CS, CL, MO and for CL versus MO, CS; repeated measures ANOVA). The effectiveness of the reduction in scattering with the CL fluctuated more from eye to eye than in the other conditions (NK1, MO, and CS). This result was statistically tested with a bootstrap algorithm comparing the minimum–maximum difference of 5000 bootstrap samples, which showed a significant increase in CAHM intereye variability when using the CL compared with that obtained with the NK1, MO, and CS ($P < 0.001$ for all three comparisons).

Therefore, possible systematic changes in the scattering present throughout the course of the experiment where explored. During data collection, the eyes were numbered in the progressive order in which they were measured (starting with eye 2). In fact, we observed systematic changes in the amount of scattering measured as a function of the eye or, equivalently, as a function of the time when the data were collected (Fig. 4). Apart from NK2, they all showed a strong correlation with time of acquisition. The correlation coefficient (r^2) between eye and experimental condition were as follows: NK1 = −0.98, NK2 = 0.56, MO = 0.89, CL = 0.99, and CS = −0.9. However, when considering the small overall variation with MO and CS (Fig. 3f), these changes become much less relevant. The stepwise increase in CAHM for the CL and the decrease in the NK1 were more prominent and will be discussed later. Repeating the scattering analysis over the whole 3.3-mm circular pupil instead of the square inscribed into the pupil did not significantly change the results.

Wavefront Sensing

The wavefront aberrations were measured for all five conditions. The second measurement of the naked eye (NK2) served as an internal control. The analysis of the wavefront aberrations in individual Zernike terms is shown in Figures 5a–c. Each condition is always plotted together with NK1 which serves as a baseline measurement. A small triangle above each Zernike

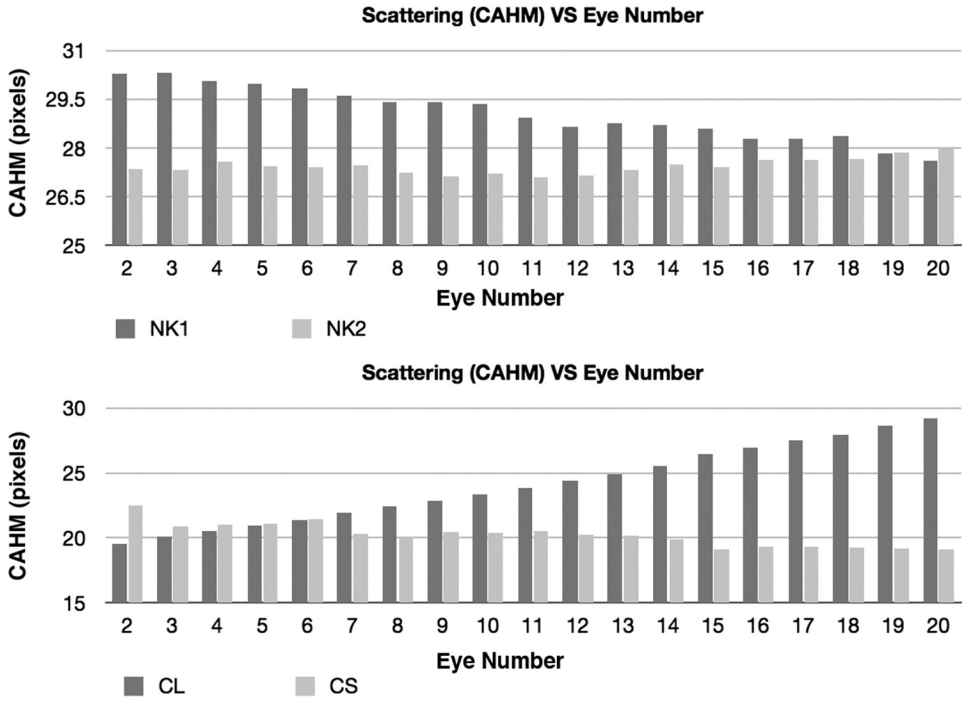

FIGURE 4. Systematic changes in scattering with time. The *x*-axis shows the eye number in the experimental order. Animal 2 was the first and animal 20 the last to be measured. *Top*: naked eyes 1 and 2; *bottom*: CL and CS. (Note the difference in the scale on the *y*-axes).

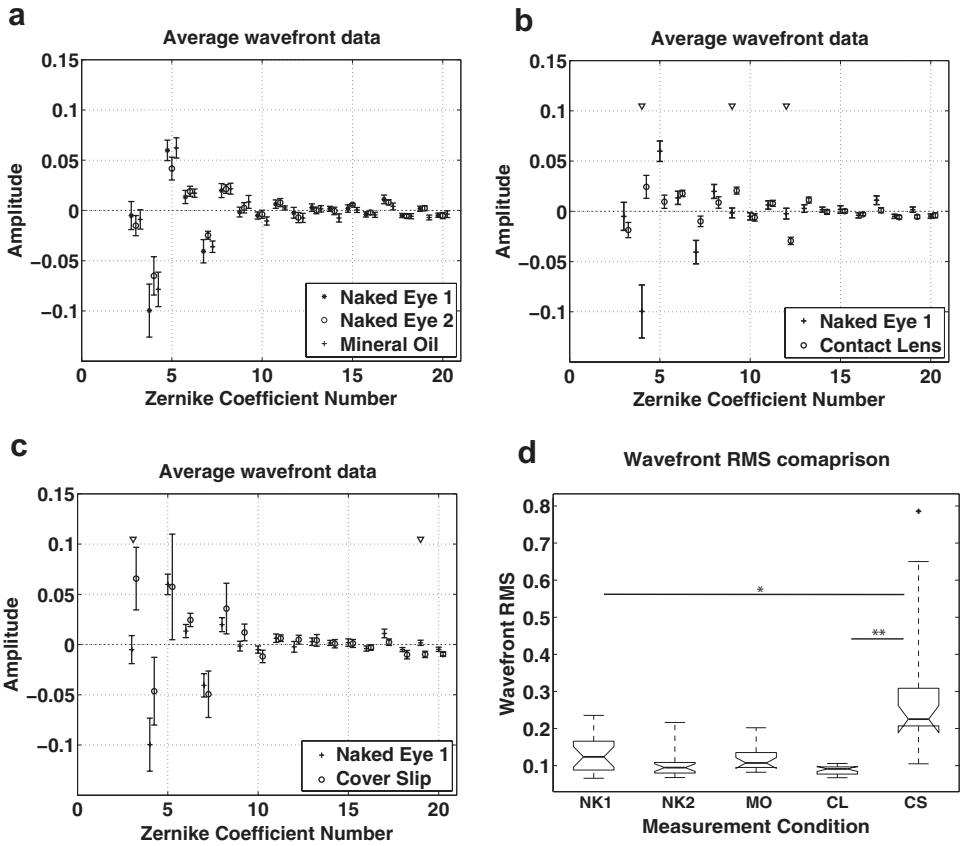

FIGURE 5. (**a**–**c**) Wavefront aberrations on the sensor's pupil plane plotted as individual Zernike coefficients; mean and SEM; $n = 19$; ▽, significant differences ($P < 0.05$). (**d**) Total wavefront RMS without defocus of all conditions. Box edges are the 25th and 75th percentiles. The error bars extend the maximum and minimum values, except + signs, denoting outliers. The wavefront RMS between CS and NK1 and between CS and CL are significantly different ($P < 0.01$ and 0.001, respectively).

term highlights a significant difference for that particular term ($P < 0.05$, one-way ANOVA with Bonferroni correction) between the two conditions. In Figure 5d the wavefront error is summarized to one value, the wavefront root mean square (RMS). The data are presented in box plots, as they did not follow a Gaussian distribution. The wavefront RMS for the different conditions were compared by Friedman test with the Dunn correction for multiple comparison.

The results in Figure 5a show a negative defocus term (-0.1 ± 0.02 μm or -0.25 ± 0.05 D) with positive 90° Zernike astigmatism (0.06 ± 0.01 μm or 0.15 ± 0.02 D), corresponding with with-the-rule astigmatism. Likewise, coma (Z_7 and Z_8) and one of the trefoil (Z_6) aberrations presented non-0 values. In particular, spherical aberration (Z_{12}) was not significantly different from 0. The comparison of NK1 and NK2 (Fig. 5a) which represent two independent measurements within the same session, showed no significant difference for any of the Zernike terms, and consequently, the wavefront RMS did not show significant differences in this case (Fig. 5d; $P > 0.05$). The use of MO (Fig. 5a) did not cause a change in the aberration profile compared with the naked eye. Accordingly, the wavefront RMS for this condition (Fig. 5d) was not significantly different from NK1 (NK1 vs. MO; $P > 0.05$).

The use of a CL, however (CL, Fig. 5b), reduced the amplitude as well as the interanimal variability (smaller error bars) of many of the individual aberration Zernike terms. The mean defocus (Z_4) was significantly lower than for NK1. Similarly, 90° astigmatism and *y*-axis coma (Z_5 and Z_7) showed a trend toward a smaller amplitude. In contrast, Z_9 (trefoil) and, very important, spherical aberration (Z_{12}) showed a small increment with the CL. Visual inspection also showed that the variability appeared smaller for all lower order aberrations (although this finding was not statistically verified). We observed a similar trend in the reduction of aberration amplitude and variability when using the CL in the wavefront RMS (Fig. 5d); however, the difference in RMS amplitudes (NK1 vs. CL) did not reach statistical significance ($P > 0.05$).

Using a CS on the eye surface significantly increased the aberrations. Z_3 (45° astigmatism) and Z_{19} were significantly higher than those for NK1. More generally, we observed a trend toward higher values of most aberrations of lower than third-order (Z_4–Z_9) with the CS, although they were not statistically significant, probably because of the larger error bars present in the CS measurements. Not surprisingly, the overall mean wavefront RMS was also significantly larger with the CS (Fig. 5d; $P < 0.01$). Visual inspection showed that the variability of all lower order aberrations, except Z_6 (coma), was higher, and similarly, the bootstrap analysis showed that the spread of the RMS was larger with the CS ($P = 0.001$).

When the best-performing methods for scattering reduction (i.e., CL and CS) were compared, the mean wavefront aberration RMS of the CS was significantly larger than the CL ($P < 0.001$). Finally, the variance of the data was also greater for the CS than for the CL ($P < 0.001$).

Optical Performance

The impact of the different air–cornea interfaces on image quality, due to aberrations alone, can be rapidly visualized with the help of the modulation transfer function (MTF), as shown in Figure 6. For a direct comparison between all measuring conditions, the mean MTF for each case (as a function of cycles per degree) is shown in Figure 6a. Figures 6b–f show the MTF (mean and SEM) for the individual air–cornea interfaces with the diffraction-limited MTF as a reference. Analogous to Figure 5d, the CL was closest to the diffraction-limited MTF and the CS farthest away. The variability of the performance, as denoted by the size of the error bars, was highest for the CS only at

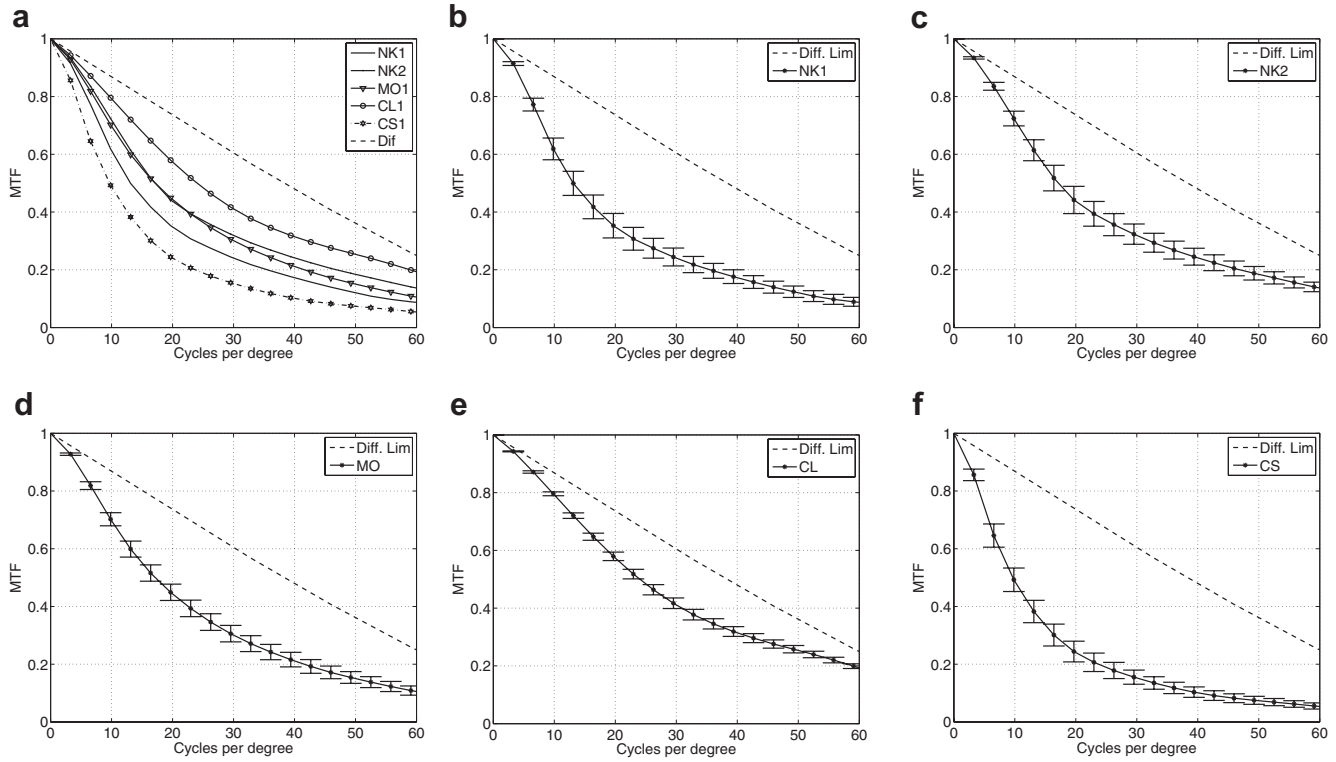

Figure 6. MTF plotted as a function of cycles per degree. (**a**) All cases are plotted for comparison (mean of $n = 19$). (**b–f**) MTF of the individual cases plotted with mean and SEM. *Dotted line*: the diffraction-limited MTF; $n = 19$.

lower spatial frequencies. At higher spatial frequencies, the MO case showed the highest variability.

Discussion

In this work, we compared the optical properties of the most commonly used methods to create a stable air–cornea interface for in vivo ocular imaging in rodents. The optical properties of the system formed by the eye, its air–cornea interface, and the group of lenses L3 when present (Fig. 1), dictate the maximum resolution that can be achieved when imaging the retina. Of particular importance is the amount of scattering and the wavefront aberrations present.

When the ability to reduce scattering was compared, the CS performed much better than any other condition. The CL was second in performance, showing a particularly large variability. Figure 4 (bottom panel) shows, however, that during the early experiments the amount of scattering present with the CL was similar to that found with the CS. The most likely explanation is that we used a new CS for each experiment but rinsed and reused the expensive custom-made CL. Therefore, despite careful cleaning, scratches, and deposits may have accumulated on the CL, leading to an increase in scattering over time. The use of a new CL after a few measurements or more thorough cleaning procedures would very likely lead to much better results in terms of scattering.

Quantification of forward light-scattering based on HS spot images is restricted to the small angle scattering ($<1°$ from the center of the PSF). The use of a specially designed double-pass system instead could have slightly increased the angle covered.[10] To truly quantify the large angle domain or straylight (1° to 100° from the center of the PSF) a separate measurement with a different device would have been necessary, which was not possible in our experimental setting. Nevertheless, our measurement setup was sufficiently sensitive to demonstrate differences in scattering between conditions. The systematic increase of the CAHM value (Fig. 4) in the CL case discussed above strongly indicates that the method indeed quantifies forward-scattering derived from the optical media. Given the purpose of the study, to determine the method of best protecting the cornea and maximizing resolution in retinal imaging, a full characterization of wide-angle scattering in the rat eye was beyond the scope of this work.

In our particular experimental conditions with the amount of defocus and all other aberrations measured, any changes in shape of the HS spots induced by aberrations were theoretically and experimentally verified to be negligible. A theoretical analysis of our system showed that for the effects of the first-pass PSF to be noticeable on the HS spots we should have at least 5.3 D of defocus, which is approximately 20 times larger than the average defocus values we recorded. The same applies for other higher order aberrations such as coma or trefoil. Numerical simulations of the HS spots using the actual wavefront measurements (including defocus and astigmatism) showed all HS spots to be airy disks of the same size. Finally, during our pilot data collection before these experiments (Diaz-Santana L, et al. *IOVS* 2010;51:ARVO E-Abstract 2322), we verified experimentally that the size of the spots was invariant, independent of the amount of defocus present (within the range expected). Hence, any changes observed in the HS spots in the data presented in this article were due to scattering.

In the presence of very large aberrations, or larger HS lenslet apertures, aberrations may affect the HS spot shape. In this case a deconvolution can be used to disentangle the scattering information from the aberrations[33,34]; however, one must be careful, as the wavefront information recorded under these conditions may be biased, because the accuracy with which the positions of the HS spots is determined can be severely affected by the change in shape of the HS spots. It is

generally accepted that if the shape of the spots is affected by aberrations, the HS operates outside of its dynamic range, and the data should not be used. We ensured that our system was operating within its dynamic range in all data sets.

The two independent measurements of the naked eye (NK1 and NK2), the second of which served as an internal control, showed a reduction in scattering between the first and the second set of measurements with the time between the two measurements being approximately 15 to 20 minutes. Although NK1 showed a decrease in scattering as the experiment progressed, NK2 stayed almost constant (Fig. 4). The last few eyes measured show very similar levels of scattering in both cases. We think that the period between the onset of anesthesia and the time when we started recording the data may have decreased as aligning the eye with the system became more routine. This may have reduced alterations to the corneal epithelium that occurred despite the use of lubricant eye drops.

Differences in scattering between the different interfaces could be due to changes in the optical properties of other optical elements in the eye, as a consequence of the anesthetic used. The specific optical properties and surface roughness of the CL, CS, and cornea, together with the scattering properties of the lubricant eye drops used to couple them to the cornea, are very likely to be the determinant factors in how much scattering is present. Direct measurement of these parameters, however, was outside the scope of this work.

The use of MO appears to have slightly reduced scattering, but less than the CL or the CS. We cannot provide a reasonable explanation for the slight but systematic increase in scattering as data collection progressed. The measurements needed to be collected very quickly, as breakup of the oil surface occurred faster than the normal tear film breakup. This phenomenon could be observed in the live image of the HS spots, appearing as shadows moving across the screen. Compared with the CL and CS, applying the oil to the cornea is much easier. Thus, for very short imaging sessions without aiming for highest resolution (e.g., cell counts), this method may be suitable. Alternatively, the use of highly viscous lubricant eye drops which are specially made to increase the breakup time of the tear film could in fact be superior to MO for quick image-acquisition procedures.

The wavefront aberrations of the eye were influenced in very different ways by the different air–cornea improvements. The MO had no effect compared to the naked eye. In contrast, the CL significantly reduced the wavefront aberrations, whereas the CS significantly increased them: In both cases, the effect was clearer mainly in aberrations of third or lower order. A possible explanation for the aberration increase with the CS may be that, analogous to the human eye, the internal optics may compensate for corneal aberrations.[19,35] As the CS nulls the refraction of the cornea, the internal aberrations of the eye may be uncovered, leading to an increase in total aberrations compared with the naked eye. Furthermore, lens L3, added to compensate for the loss of optical power, has an impact on the resulting wavefront's reaching the HS sensor. Improving the optical quality of L3—for example, by using a microscope objective—may decrease the aberrations measured with the CS. However, this benefit may be negligible, as the combination of lenses used in L3 was already designed to minimize aberrations in our setup. Using two microscope objectives, a Badal system could be built in an approach similar to that proposed by Artal et al.[36] Then, the focusing correction for the loss of optical power in the CS case would already be included, and addition of L3 would not be necessary. A different strategy could be to design L3 in a way that it introduces aberrations complementary to the wavefront aberrations derived from the inner eye optics and which can rotate/translate together with the rat eye ensuring an optimal coupling at all times. This approach would result in fewer total aberrations and could therefore be attractive for imaging purposes.

For practical high-resolution imaging, not only is the amplitude of the wavefront of great importance but also its variability, both as a function of eccentricity and between individuals. Large changes in the wavefront aberration amplitude from eye to eye, or even within one session when changing the imaging field, will challenge every imaging system, whether correcting methods such as AO are used or not. In other words, the less these aberrations vary, the less demanding it will be to design a system that can obtain high-resolution images over a larger field of view in a large proportion of eyes. Thus, it is an important feature of the CL that it reduces not only the aberration amplitude but also its variability. The CS, in contrast, greatly increases the aberration variability compared with all other interfaces. Previously reported work on ray tracing simulations of the rat eye, and its coupling to the CL or CS, showed that the wavefront aberrations increased rapidly with eccentricity when using a CS, but much less with the CL or naked eye. (Diaz-Santana L, et al. *IOVS* 2010;51:ARVO E-Abstract 2322). On the basis of these results, we speculate that the reason for the larger variability observed with the CS was due to misalignment of the optical axis during our experiments inducing larger wavefront aberrations, whereas similar misalignments with the CL did not translate into larger wavefront errors. That is, the CL appears to be more tolerant to eccentric imaging. Imaging eccentric to the optical axis often occurs in live imaging, not by accident but deliberately when attempting to reach more peripheral areas of the retina. Therefore, the CL may have a clear advantage over the other methods, especially the CS, as it reduces the aberration amplitude, increases the predictability of the wavefront aberrations and, consequently, the image quality. Further experimental work is necessary to confirm that it is indeed more tolerant to eccentric imaging. The disadvantage in scattering reduction may be overcome by using a new or thoroughly cleaned lens after a few imaging sessions.

To illustrate the practical implications of both aberrations and scattering on image quality, we include as part of this discussion numerical simulations of image formation under some of the different conditions measured. They are limited by the assumptions made to estimate the effects of scattering and by the mathematical formalism used (Fraunhofer approximation). They should not be treated as strict predictions, but as an aid to understand our results.

Details of how the simulations were performed are presented in Appendix A. The original image (Fig. 7A) used for these simulations shows a fluorescent retinal ganglion cell in a flat-mounted retina from a YFPH transgenic mouse. Each pixel in the image measures 0.5 μm. Figure 7D shows the effects of diffraction alone. An ideal rat eye without either aberrations or scattering would produce such an image. The blurring observed is due to the wave nature of light alone. In this case, the experimental width of the SH spots provided by the manufacturer gave an area CAHM = 7.5.

The two center panels (Figs. 7B, 7E) show the effect of the aberrations measured with the CL in eye 3, while the rightmost panels (Figs. 7C, 7F) show the effect of aberrations in this same eye when using the CS. In the top panels (Figs. 7B, 7C) the minimum amount of scattering measured in all the experiments (CAHM = 19.11) was used, while in the bottom panels (Figs. 7E, 7F), we used the maximum amount of scattering measured (CAHM = 30.28). When comparing the images, it becomes apparent that aberrations have a dominant role. In the CS case, the effect of scattering is practically invisible compared with the degradation introduced by aberrations alone. In the case of the CL, the two values of scattering used result in

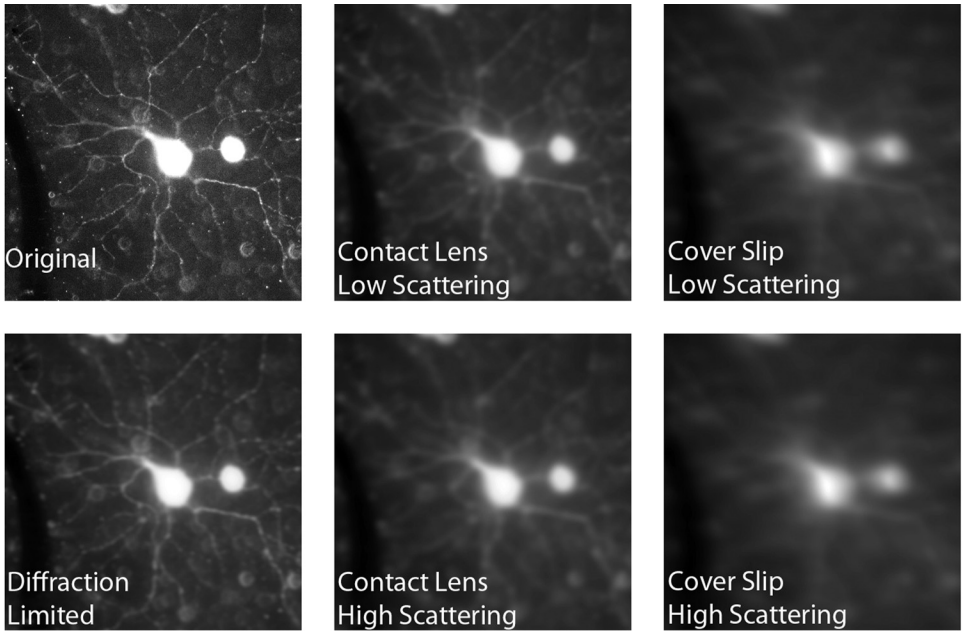

FIGURE 7. Simulated effects of scattering and aberrations on image formation using an image of a retinal ganglion cell in a flat-mounted retina of a YFPH transgenic mouse. *Top*, *left* to *right*: original image, CL aberrations from eye 3 with minimum scattering measured, and CS aberrations from eye 3 with minimum scattering measured. CAHM = 19.11 in both cases. *Bottom*: *left* to *right*: diffraction-limited image (no aberrations and no scattering), CL aberrations from eye 3 with maximum scattering measured, and CS aberrations from eye 3 with maximum scattering measured. CAHM = 30.28 in both cases. The wavefront RMS of eye 3 was close to average for both the CL and the CS measurements.

a very small difference in contrast. Scattering, however, still prevents us from reaching the optimal quality of a diffraction-limited image, even in the absence of aberrations.

For practical high-resolution in vivo imaging experiments, obtaining good-quality images in a reliable manner is of fundamental importance. Considering this, we conclude from our study that using a CL is the best way to create a stable, optically improved air–cornea interface.

Acknowledgments

The authors thank Eyeart for accommodating the demands for the design of the contact lenses, Michael Bach and Sven Heinrich for advice on the use of bootstrap algorithms, and the City University and University of Cambridge for their support of LD-S during his sabbatical year at the Cambridge Centre for Brain Repair, Cambridge University, when this research was performed.

APPENDIX

Mathematics of the Image Simulations

We used the image of a perfect array of HS spots without any aberrations nor scattering (provided by the manufacturer of the HASO sensor; Imagine Eyes) to define the width of the HS spots under perfect conditions. Using this image, we measured the CAHM of the perfect spots to be 7.5 pixels in area. Compare this with the best values, close to 18, with the CS (Fig. 4).

The effects of scattering and aberrations can be combined via convolution, as described by Donnelly et al.[33] and others[9,37] Mathematically it is simpler to deal with a convolution in the frequency domain, as the convolution of two functions becomes a product of their Fourier transforms in the frequency space. The optical contribution is the PSF and its Fourier transform the optical transfer function (OTF). The module or magnitude of the OTF is the MTF of the optical system. We can define a new transfer function that combines the effects of scattering and aberrations by multiplying the MTF and the scattering transfer function (STF) to create a new, generalized transfer function that includes the effects of both scattering and aberrations, and we will denote it as TT. Note that these functions exist in the frequency domain, and hence are functions of (μ,ν).

$$TT(\mu, \nu) = MTF(\mu, \nu) \times STF(\mu, \nu). \quad (1)$$

From the perfect images of the HS spots, it is possible to obtain the MTF for a perfect system. In the absence of scattering, the TT must be equal to the MTF, as only aberrations affect image quality. Hence, necessarily STF = 1 for all frequencies. We know that, given the way we measured aberrations in an asymmetric double pass,[29] the HS spots are not affected by aberrations. Hence, from the HS spots of the measured eyes we can estimate TT.

$$STF(\mu, \nu) = TT(\mu, \nu)/MTF(\mu, \nu). \quad (2)$$

If the Fourier transform of the object to be imaged is

$$FT\{O\} = \hat{o}(\mu, \nu) \quad (3)$$

and the optical transfer function of the eye in question is calculated from its PSF as

$$OTF(\mu, \nu) = FT\{PSF(x, y)\} \quad (4)$$

then the image produced by the eye including scattering is

$$Im_{out}(x, y) = FT^{-1}\{STF(\mu, \nu) \times OTF(\mu, \nu) \times \hat{o}(\mu, \nu)\} \quad (5)$$

where $FT^{-1}\{\}$denotes the inverse Fourier transform.

We used equation 5 to simulate image performance. The OTF was directly calculated from our wavefront data. An image collected with a fluorescence microscope of a retinal ganglion cell in a flat-mounted retina was used to simulate performance. Scaling was such that each pixel on the PSF and the image corresponded with 0.5 μm in real space.

References

1. Seeliger M, Beck S, Pereyra-Munoz N, et al. In vivo confocal imaging of the retina in animal models using scanning laser ophthalmoscopy. *Vision Res.* 2005;45:3512–3519.

2. Walsh MK, Quigley HA. In vivo time-lapse fluorescence imaging of individual retinal ganglion cells in mice. *J Neurosci Methods.* 2008; 169:214–221.
3. Murata H, Aihara M, Chen Y, Ota T, Numaga J, Araie M. Imaging mouse retinal ganglion cells and their loss in vivo by a fundus camera in the normal and ischemia-reperfusion model. *Invest Ophthalmol Vis Sci.* 2008;49:5546–5552.
4. Leung CKS, Weinreb RN. Experimental detection of retinal ganglion cell damage in vivo. *Exp Eye Res.* 2009;88:831–836.
5. de la Cera EG, Rodriguez G, Llorente L, Schaeffel F, Marcos S. Optical aberrations in the mouse eye. *Vision Res.* 2006;46:2546–2553.
6. van Oterendorp C, Martin K, Zhong J, Diaz-Santana L. An ex vivo rat eye model to aid development of high-resolution retina imaging devices for rodents. *J Modern Opt.* 2010;57:1555–1563.
7. Higashide T, Kawaguchi I, Ohkubo S, Takeda H, Sugiyama K. in vivo imaging and counting of rat retinal ganglion cells using a scanning laser ophthalmoscope. *Invest Ophthalmol Vis Sci.* 2006; 47:2943–2950.
8. Geng Y, Greenberg K, Wolfe R, et al. In vivo imaging of microscopic structures in the rat retina. *Invest Ophthalmol Vis Sci.* 2009;50:5872–5879.
9. Pinero D, Ortiz D, Alio J. Ocular scattering. *Optom Vis Sci.* 2010; 87:E682–E696.
10. van den Berg T, Franssen L, Coppens J. Straylight in the human eye: testing objectivity and optical character of the psychophysical measurement. *Ophthalmic Physiol Opt.* 2009;29:345–350.
11. Guirao A, C Gonzalez MR, Geraghty E, Norrby S, Artal P. Average optical performance of the human eye as a function of age in a normal population. *Invest Ophthalmol Vis Res.* 1999;40:203–213.
12. Westheimer G, Liang J. Influence of ocular light scatter on the eye's optical performance. *J Opt Soc Am A.* 1995;12:1417–1424.
13. Applegate R, Thibos L. Methods and systems for measuring local scattering and aberration properties of optical media. U.S. Patent. 6905210; 2005.
14. Fujikado T, Kuroda T, Maeda N, et al. Light scattering and optical aberrations as objective parameters to predict visual deterioration in eyes with cataracts. *J Cataract Refract Surg.* 2004;30:1198–1208.
15. Seery L, McLaren J, Kittleson K, Patel SV. Retinal point-spread function after corneal transplantation for Fuchs' dystrophy. *Invest Ophthalmol Vis Sci.* 2011;52:1003–1008
16. Kuroda T, Fujikado T, Ninomiya S, Maeda N, Hirohara Y, Mihashi T. Effect of aging on ocular light scatter and higher order aberrations. *J Refract Surg.* 2002;18:S598–S602.
17. Donnelly W. *Measuring and Modeling Intraocular Light Scatter with Shack-Hartmann Wavefront Sensing and the Effects of Nuclear Cataract on the Measurement of Wavefront Error.* PhD thesis. Houston, TX: University of Houston; 2005.
18. Cervino A, Bansal D, Hosking SL, Montes-Mico R. Objective measurement of intraocular forward light scatter using Hartmann-Shack spot patterns from clinical aberrometers: model-eye and human-eye study. *J Cataract Refract Surg.* 2008;34:1089–1095.
19. Campbell MCW, Hughes A. An analytic, gradient index schematic lens and eye for the rat which predicts aberrations for finite pupils. *Vision Res.* 1981;21:1129–1148.
20. Tyson R. *Principles of Adaptive Optics.* 2nd ed. San Diego, CA: Academic Press; 1991.
21. Liang J, Williams D. Supernormal vision and high resolution retinal imaging through adaptive optics. *J Opt Soc Am A.* 1997;14:2884–2892.
22. Roorda A, Williams D. The arrangement of the three cone classes in the living human eye. *Nature.* 1999;397:520–522.
23. Roorda A, Romero-Borja F, Donnelly W, Queener H, Hebert T, Campbell M. Adaptive optics scanning laser ophthalmoscopy. *Opt Express.* 2002;10:405–412.
24. Hermann B, Fernandez EJ, Unterhuber A, et al. Adaptive-optics ultrahigh-resolution optical coherence tomography. *Opt Lett.* 2004;29:2142–2144.
25. Zhang Y, Rha JT, Jonnal RS, Miller DT. Adaptive optics parallel spectral domain optical coherence tomography for imaging the living retina. *Opt Express.* 2005;13:4792–4811.
26. Burns S, Tumbar R, Elsner A, Ferguson D, Hammer D. Large-field-of-view, modular, stabilized, adaptive-optics-based scanning laser ophthalmoscope. *J Opt Soc Am A.* 2007;24:1313–1326.
27. Romero-Borja F, Venkateswaran K, Roorda A, Hebert T. Optical slicing of human retinal tissue in vivo with the adaptive optics scanning laser ophthalmoscope. *Appl Opt.* 2005;44:4032–4040.
28. Liang J, Grimm B, Goelz S, Bille J. Objective measurement of wave aberration of the human eye with the use of a Hartmann-Shack wave-front sensor. *J Opt Soc Am A.* 1994;11:1949–1957.
29. Artal P, Marcos S, Navarro R, Williams D. Odd aberrations and double pass measurements of retinal image quality. *J Opt Soc Am A.* 1995;12:195–201.
30. Talmi A, Ribak E. Direct demodulation of hartmann-shack patterns. *J Opt Soc Am A Opt Image Sci Vis.* 2004;21:632–639.
31. ANSI. *American National Standard for Ophthalmics.* ANSI-Z80.28-2004, Methods for reporting optical aberrations of eyes. Washington, DC: American National Standards Institute, Inc.; 2004.
32. Goodman J. *Introduction to Fourier Optics.* 2nd ed. McGraw-Hill, Singapore; 1996.
33. Donnelly W, Pesudovs K, Marsack J, Sarver E, Applegate R. Quantifying scatter in Shack-Hartmann images to evaluate nuclear cataract. *J Refract Surg.* 2004;20:S515–522.
34. Shahidi M, Yang Y, Rajagopalan A, Alexander K, Zelkha R, Fishman G. A method for differentiating ocular higher-order aberrations from light scatter applied to retinitis pigmentosa. *Optom Vis Sci.* 2005;82:976–980.
35. Artal P, Benito A, Tabernero J. The human eye is an example of robust optical design. *J Vision.* 2006;6:1–7.
36. Artal P, Guirao A, Berrio E, Williams DR. Compensation of corneal aberrations by the internal optics in the human eye. *J Vision.* 2001;1:1–8.
37. Shahidi M, Yang Y. Measurements of ocular aberrations and light scatter in healthy subjects. *Optom Vis Sci.* 2004;81:853–857.